## Electron Cyclotron Maser Emission as the Driving Mechanism in Long-Period Radio Transients

Lilia Ferrario<sup>1</sup>\*

<sup>1</sup> Mathematical Sciences Institute, The Australian National University, Canberra, ACT 2601, Australia

Accepted XXX. Received YYY; in original form ZZZ

### ABSTRACT

Long-period radio transients (LPRTs) are highly polarised, coherent radio sources with periods of minutes to hours and bursts typically lasting  $10-100\,\mathrm{s}$ . We argue that electron cyclotron maser emission (ECME) explains their narrow duty cycles and polarisation properties. In this picture, a rotating oblique magnetosphere beams radiation into a thin, hollow emission cone whose surface lies almost perpendicularly to the local magnetic field. The observed very narrow pulses arise when the line of sight skims the cone. Broader profiles and weak leading or trailing components occur when multiple azimuths along the emission ring satisfy the maser resonance condition. The observed isotropic-equivalent luminosities of  $\sim 10^{30}-10^{31}\,\mathrm{erg\,s^{-1}}$  correspond to modest intrinsic powers once strong ECME beaming is taken into account, which is readily achievable through accretion from the interstellar medium.

**Key words:** radio continuum: transients – stars: neutron – white dwarfs – stars: magnetic fields – masers – radiation mechanism: non-thermal

## 1 INTRODUCTION

LPRTs are sources with spin periods of minutes to hours that produce highly polarised bursts. Their periodicities and polarisation fractions distinguish them from ordinary pulsars and magnetars, strongly suggesting different emission mechanisms. Also, their inferred brightness temperatures,  $\gtrsim 10^{16}$  K, require a coherent emission mechanism. Peak flux densities are in the range 0.1-40 Jy, implying isotropic-equivalent radio luminosities of  $\sim 10^{30}-10^{31}$  erg s<sup>-1</sup> for typical distances of  $\sim 1-5$  kpc (Rea et al. 2024).

The prototypical source, GLEAM-X J1627 – 5235 (Hurley-Walker et al. 2022), shows strongly linearly polarised (up to nearly 90 per cent) bursts lasting  $30-60\,\mathrm{s}$  every 18.18 min. Subsequent discoveries include GPM J1839 – 10 ( $P=21\,\mathrm{min}$ ; Hurley-Walker et al. 2023), ASKAP J1755 – 2527 (Dobie et al. 2024), ASKAP J1935 + 2148 (Caleb et al. 2024) ( $P=53.8\,\mathrm{min}$ ), and ASKAP J1839 – 0756 (Lee et al. 2025) ( $P=6.45\,\mathrm{h}$ ) showing a weaker interpulse separated by half a rotation. A further source, ASKAP/DART J1832 – 0911 emits two-minute radio bursts every 44 min that are accompanied by phase-aligned X-ray pulses (Li et al. 2024; Wang et al. 2025) .

Despite differences in period and polarisation characteristics, LPRTs share several features: (i) extremely high brightness temperatures, (ii) lack of emission at other wavelengths (with the exception of ASKAP J1832 - 0911), (iii) high and variable polarisation, and (iv) long-term phase stability. These properties make standard pulsar or magnetar interpretations rather difficult. Canonical dipole spin-down cannot

produce neutron stars with spin periods of minutes to hours within the age of the Galaxy unless the neutron star possesses ultra-strong magnetic fields ( $B_* \gtrsim 10^{15} \, \mathrm{G}$ ) that do not decay significantly over time. Standard particle-acceleration mechanisms in isolated neutron stars or magnetic white dwarfs (MWDs) with rotating dipoles also fail to explain the observed radio emission characteristics (see Rea et al. 2024).

Given the narrow duty cycles of LPRTs, stable periodicities, and high polarisation, the ECME mechanism could be the most convincing explanation. ECME is established as the mechanism powering auroral radio emission in planets and magnetic stars (Zarka 1998; Leto et al. 2016; Trigilio et al. 2011; Leto et al. 2021). It has also been observed in magnetic cataclysmic variables (MCVs, Ferrario et al. 2020; Barrett et al. 2020) and in WD pulsars like AR Scorpii (Marsh et al. 2016). ECME has also been proposed for some coherent burst classes in solar flares (e.g. Treumann 2006; White et al. 2024).

In LPRTs, ECME likely originates in the outer magnetospheres of neutron stars or MWDs where the local field satisfies (as first derived by Wu & Lee 1979, in relation to the terrestrial auroral kilometric radiation)

$$\nu_{\rm ce} \approx 2.8\,{\rm MHz}\left(\frac{B}{1\,{\rm G}}\right),$$

so that GHz emission corresponds to  $B \sim 10^2-10^3$  G. Such field strengths occur at radii of tens to hundreds of stellar radii, depending on the surface magnetic field of the star.

ECME requires a continuous supply of mildly relativistic electrons to sustain maser growth. As most LPRTs show no evidence of a companion star or of emission at other wavelengths, apart from one exceptional case, we propose that the

<sup>\*</sup> E-mail: lilia.ferrario@anu.edu.au

necessary particle replenishment comes from the capture of interstellar material.

The possibility of accretion from the interstellar medium (ISM) was originally proposed by Ostriker et al. (1970) as a way to detect extinct pulsars via their soft X-ray emission. The detection of X-rays from ASKAP J1832 – 0911 is consistent with weak, magnetically channelled accretion from the ISM that simultaneously powers the radio bursts and the high-energy emission.

In what follows, we present an ECME interpretation for LPRTs. Section 2 summarises the maser mechanism and its geometrical implications. Section 3 discusses the origin of their polarisation diversity. Section 4 discusses how neutron stars can reach the long spin periods of LPRTs and the possible power source. We discuss our results in Section 5, while Section 6 summarises the paper.

### 2 ELECTRON CYCLOTRON MASER EMISSION

Here we summarise the geometry, while background information on ECME is provided in Appendix A.

This maser mechanism operates under the following resonance condition Wu & Lee (1979):

$$\omega - k_{\parallel} v_{\parallel} - \frac{n \Omega_e}{\gamma} = 0, \tag{1}$$

where  $\omega$  is the wave angular frequency,  $k_{\parallel}$  is the component of the wavevector **k** parallel to the local magnetic field **B**,  $v_{\parallel}$  is the component of the particle's velocity **v** parallel to **B**,  $\Omega_e = eB/(m_ec)$  is the electron gyrofrequency,  $\gamma$  is the Lorentz factor, and  $n=1,2,3,\ldots$  is the cyclotron harmonic number.

Maximum growth occurs for quasi-transverse propagation, that is, the emission peaks at  $\theta_{Bk} \simeq 90^{\circ} - \delta\theta$ , where  $\theta_{Bk}$  is the angle between **k** and **B**. The small offset  $\delta\theta$  (typically a few degrees) arises from propagation effects. The finite wall thickness  $\sigma$  of the hollow cone, typically  $\lesssim 1^{\circ}$ , traces the angular width over which the growth rate remains significant.

Efficient maser amplification requires a low plasma density such that  $\omega_p/\Omega_e \lesssim 0.1-0.3$ , where  $\omega_p=(4\pi n_e e^2/m_e)^{1/2}$  is the plasma frequency. In this regime, the fundamental harmonic is favoured and the emitted radiation can propagate out of the source region without strong absorption (Treumann 2006).

The so-called "loss cone" is the deficit of electrons at small pitch angles produced by magnetic mirroring (see Appendix A). Particles with insufficient perpendicular momentum stream along the field lines and precipitate into the stellar surface, leaving a depletion in the distribution  $f(v_{\parallel},v_{\perp})$  at low  $v_{\perp}$ . This creates the positive perpendicular gradient required for maser growth. Consequently, the growth rate in velocity space is proportional to the gradient  $\partial f/\partial v_{\perp}$  of the electron distribution, so the maser amplifies radiation most efficiently where the resonance curve samples regions of positive perpendicular gradient. This is illustrated in Figure 1, which summarises how the cyclotron resonance ellipse intersects the loss-cone boundary near  $v_{\parallel} \simeq 0$ , selecting quasitransverse propagation and thereby maximising the maser gain.

The characteristic field at the emission site (see Ap-

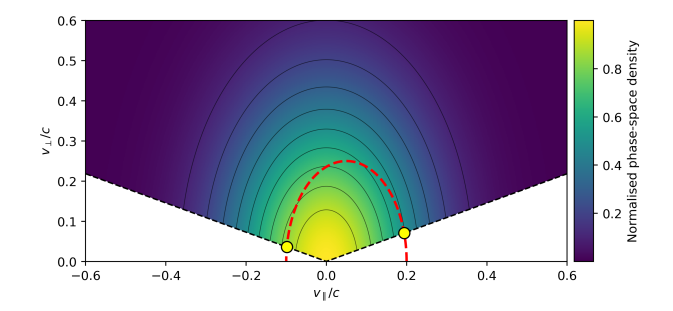


Figure 1. Resonance loss-cone geometry in  $(v_{\perp}, v_{\parallel})$ . Colour shading shows a bi-Maxwellian with symmetric loss cones (interior excised). Dashed lines mark the loss-cone edge  $v_{\perp} = |v_{\parallel}| \tan \alpha_{\rm L}$ . The red curve is a representative cyclotron resonance ellipse for fixed  $(\omega, k_{\parallel})$  and harmonic n. Yellow circles indicate the intersections where the resonance reaches the largest positive  $\partial f/\partial v_{\perp}$ , maximising maser growth at quasi-transverse propagation  $(k_{\parallel} \simeq 0)$ .

pendix A) is

$$B_{\rm loc}[{\rm G}] \simeq 357 \frac{\gamma}{n} \nu_{\rm obs}[{\rm GHz}].$$
 (2)

Thus, for  $\nu_{\rm obs}$  in the range  $1.0-1.4\,{\rm GHz},\ n=1-2,$  and  $\gamma\simeq 1.1-2,$  the inferred field strengths  $(B_{\rm loc}\sim 10^2-10^3\,{\rm G})$  place the GHz ECME layer at radii of tens to hundreds of stellar radii in both neutron stars and MWDs, since for a dipole

$$\frac{r}{R_*} = \left(\frac{B_*}{B_{\text{loc}}}\right)^{1/3}.\tag{3}$$

As the star rotates, the emission cone whose axis is aligned with  $\mathbf{B}_{\mathrm{loc}}$  sweeps across the observer's line of sight. Pulses occur when the line of sight intersects the cone wall (see Section 2.1).

## 2.1 Geometry and visibility

ECME is detected only when the beaming angle  $\theta_{Bk}$  lies close to the characteristic cone angle  $\theta_{\text{cone}}$  where maser growth is strongest, so visibility depends sensitively on the observer's line of sight and on the magnetic obliquity  $\beta$ .

To show this, we adopt a right-handed reference frame with the stellar spin axis along  $\hat{\mathbf{z}}$ . The observer's inclination i is the angle between the line of sight  $\hat{\mathbf{n}}_{\text{obs}}$  and  $+\hat{\mathbf{z}}$ ,

$$\hat{\mathbf{n}}_{\text{obs}} = (\sin i, 0, \cos i), \qquad 0 \le i \le \pi.$$

We denote  $\beta$  the angle between the magnetic axis  $\hat{\mathbf{m}}$  and  $+\hat{\mathbf{z}}$ . Thus, as the star rotates, the magnetic axis precesses around  $\hat{\mathbf{z}}$ :

$$\hat{\mathbf{m}}(\phi) = (\sin \beta \cos \phi, \sin \beta \sin \phi, \cos \beta), \tag{4}$$

where  $\phi$  is the rotational phase and  $\phi = 0$  occurs when  $\hat{\mathbf{m}}$  is in the plane defined by  $\hat{\mathbf{z}}$  and  $\hat{\mathbf{n}}_{\text{obs}}$ .

All points on the emission ring where  $B = B_{loc}$  (equation 2), are traced by the vector

$$\hat{\mathbf{r}}(\phi, \phi_m) = \sin \theta_m [\cos \phi_m \hat{\mathbf{e}}_1(\phi) + \sin \phi_m \hat{\mathbf{e}}_2(\phi)] + \cos \theta_m \hat{\mathbf{m}}(\phi). \tag{5}$$

Here  $\theta_m$  is the magnetic colatitude of the emission ring, and the unit vectors  $\hat{\mathbf{e}}_1$  and  $\hat{\mathbf{e}}_2$  span the plane perpendicular to  $\hat{\mathbf{m}}(\phi)$ .

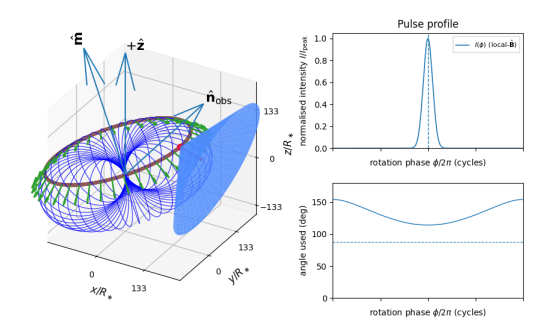


Figure 2. Schematic of the ECME emission geometry in an oblique rotator. The spin axis  $\hat{\mathbf{z}}$  defines the rotation frame, while the magnetic axis  $\hat{\mathbf{m}}$  is tilted relative to it by an angle  $\beta$ . The observer's line of sight  $\hat{\mathbf{n}}_{\text{obs}}$  makes an inclination i to the spin axis. Magnetic field lines (depicted in blue) illustrate the dipolar topology. ECME arises where the local magnetic field equals the resonance value  $B_{\text{loc}}$ . Here a hollow emission cone (shaded), centred on  $\hat{\mathbf{b}}$  and with opening angle  $\theta_{\text{cone}}$ , is formed. As the star rotates, the hollow cone sweeps past the observer, producing one or two pulses per rotation depending on geometry. The right panels illustrate the resulting pulse profile and the phase variation of  $\theta_{Bk}$ .

For a centred dipole, the local field direction is

$$\hat{\mathbf{b}}(\phi, \phi_m) = \frac{3(\hat{\mathbf{m}} \cdot \hat{\mathbf{r}})\hat{\mathbf{r}} - \hat{\mathbf{m}}}{\|3(\hat{\mathbf{m}} \cdot \hat{\mathbf{r}})\hat{\mathbf{r}} - \hat{\mathbf{m}}\|},\tag{6}$$

and the instantaneous beaming angle is

$$\theta_{Bk}(\phi, \phi_m) = \arccos[\hat{\mathbf{b}}(\phi, \phi_m) \cdot \hat{\mathbf{n}}_{\text{obs}}]. \tag{7}$$

Figure 2 illustrates this geometry. The ECME cone's axis is aligned with the local field direction  $\hat{\mathbf{b}}$  and has an opening angle  $\theta_{\text{cone}}$ . As the star rotates, the cone sweeps past the observer. Depending on  $(i, \beta)$  and the width of the cone wall,  $\sigma$ , the line of sight may intersect the beaming surface once per rotation (a single pulse), twice (an interpulse), or not at all. It is also possible for multiple azimuths along the emission ring to satisfy the resonance condition, producing leading or trailing weaker components in addition to the main pulse(s).

Emission is detectable when

$$|\theta_{Bk}(\phi, \phi_m) - \theta_{\text{cone}}| \lesssim \sigma.$$
 (8)

The observed duty cycle  $\Delta t/P$  is determined by how long the line of sight intersects the thin emission wall of the hollow cone as the star rotates. To first order,

$$\frac{\Delta t}{P} \simeq \frac{\sigma}{\sin i \, \sin \zeta_{\text{loc}}},\tag{9}$$

where  $\zeta_{\rm loc}$  is the angle between the spin axis and the local magnetic-field direction at the emitting field line. Very small duty cycles arise from thin cone walls ( $\sigma \simeq 0.3^{\circ} - 0.5^{\circ}$ ) and geometries with  $\sin i \sin \zeta_{\rm loc} \approx 1$ .

An antipodal magnetic pole may generate an interpulse separated by approximately half a rotation. Whether both hemispheres contribute to the observed radiation depends on the plasma distribution and its propagation toward the observer. Emission from one hemisphere can be strongly attenuated if it traverses a denser magnetised plasma column. Extending the geometric model to two poles simply requires adding the contribution from the antipodal emission region.

Because  $\nu \propto B \propto r^{-3}$ , lower frequency emission originates at larger radii. This produces a small, systematic shift in the rotational phase at which the hollow cone intersects the line of sight. Thus, multi-band radio pulse phases probe both the surface field strength and the radial field gradient, since each observing band samples a different ECME resonance height set by  $B(r) = B_{loc}(\nu)$ .

## 3 POLARISATION DIVERSITY IN LPRTS UNDER THE ECME FRAMEWORK

We describe polarisation using the Stokes vector  $\mathbf{S} = (I,Q,U,V)^{\top}$ , where I is total intensity, Q and U quantify linear polarisation, and V circular polarisation. The fractional linear and circular polarisations are  $L/I = \sqrt{Q^2 + U^2}/I$  and |V|/I, respectively.

LPRTs show pulses with both large |V|/I and L/I, sometimes within the same burst. In the ECME picture, this arises from (i) intrinsic emission that favours quasi-transverse propagation, and (ii) subsequent propagation through magnetised plasma that mixes Stokes parameters, as we illustrate below.

After generation, the radiation traverses a birefringent plasma. The transfer equations in Section 3.1 show that the coefficients  $\rho_R$  and  $\rho_W$  govern Faraday rotation (mixing of Q and U) and Faraday conversion (mixing of U and V), respectively. The cumulative conversion depth

$$\tau_C = \int \rho_W \, ds \tag{10}$$

quantifies how an initially circular state acquires linear power. We likewise define the rotation depth

$$\tau_R = \int \rho_R \, ds,\tag{11}$$

which measures the net Faraday rotation of the linear polarisation angle. For homogeneous conditions,  $\tau_R \sim 1$  corresponds to a rotation of order one radian.

## 3.1 Polarised radiative transfer in Stokes form

Let  $\mathbf{S} \equiv (I,Q,U,V)^{\top}$  be the Stokes vector. We consider a plane-parallel slab, with the ray parameter s measured along the line of sight, increasing in the direction of propagation from the ECME source (s=0) to the escape point  $(s=s_{\rm esc})$ . Let  $\mathbf{S}_{\rm em}=(S_I,S_Q,S_U,S_V)^{\top}$  be the emissivity vector (erg cm<sup>-1</sup> s<sup>-1</sup> sr<sup>-1</sup> Hz<sup>-1</sup>) per unit path length. The transfer equation is

$$\frac{d\mathbf{S}}{ds} = \mathbf{S}_{em} - \boldsymbol{\eta} \, \mathbf{S},\tag{12}$$

with propagation matrix

$$\boldsymbol{\eta} = \begin{pmatrix} \eta_I & \eta_Q & \eta_U & \eta_V \\ \eta_Q & \eta_I & -\rho_R & 0 \\ \eta_U & \rho_R & \eta_I & -\rho_W \\ \eta_V & 0 & \rho_W & \eta_I \end{pmatrix}. \tag{13}$$

The first row describes total intensity attenuation. The antisymmetric off-diagonal terms encode birefringent coupling among Q, U, V. The absence of a  $\rho_U$  term follows from choosing the Stokes-Q reference axis along the projection of  $\mathbf{B}$  onto the sky.

Landi Degl'Innocenti & Landi Degl'Innocenti (1973) argued, from general principles, that the transfer equation for polarised radiation must have the above form and symmetry properties (see also Martin & Wickramasinghe 1979).

The coefficients  $\eta_I, \eta_Q, \eta_U, \eta_V$  describe extinction acting on I, Q, U, V, respectively. The term  $\eta_I$  attenuates all Stokes components equally (or amplifies them if  $\eta_I < 0$  in a maser). The terms  $\eta_{Q,U,V}$  represent dichroism. The term  $\eta_V$  (circular dichroism) is differential absorption of right- vs left-hand components and generates circular polarisation from initially linear or unpolarised light. The terms  $\eta_Q$  and  $\eta_U$  (linear dichroism) represent differential absorption between orthogonal linear axes and generate linear polarisation with the electric vector position angle (EVPA) aligned to the favoured axis.

The antisymmetric part (the  $\rho$  terms) converts one type of polarisation into another without changing I. In the absence of absorption, it preserves  $P = (Q^2 + U^2 + V^2)^{1/2}$ . The coefficient  $\rho_R$  mixes Q and U (Faraday rotation of the EVPA), while the coefficient  $\rho_W$  mixes U and V (Faraday conversion, or the Voigt effect, Martin & Wickramasinghe 1981, 1982)). In ECME, this conversion is chiefly responsible for transforming intrinsically circular output into linear output.

Therefore, we adopt the following scenario. ECME grows in a low-density cavity ( $\omega_p/\Omega_e < 0.1$ ), after which the amplified waves traverse a second region consisting of a magnetised plasma column. In this post-growth region, an initially circular ECME beam can emerge with substantial linear fractions, provided the cumulative conversion depth satisfies  $\tau_C \sim 0.1-1$ .

We model the post-growth escape through this second region using a cold plasma slab of thickness L in which the ray propagates quasi-transversely to the magnetic field, so that absorption and dichroism are negligible. We therefore set  $S_{I,Q,U,V}=0$ , require  $|\eta_{Q,U,V}|\,L\ll 1$ , and retain only the scalar extinction  $\eta_I$  and the birefringent terms. Under these conditions, the reduced Stokes system is

$$\frac{dI}{ds} = -\eta_I I,\tag{14}$$

$$\frac{dQ}{ds} = -\eta_I Q + \rho_R U,\tag{15}$$

$$\frac{dU}{ds} = -\eta_I U - \rho_R Q + \rho_W V, \tag{16}$$

$$\frac{dV}{ds} = -\eta_I V - \rho_W U. \tag{17}$$

In the cold-plasma, high-frequency limit ( $\omega \gg \omega_p, \Omega_e$ ), the birefringent coefficients are (Pacholczyk 1976):

$$\rho_R = \frac{\omega_p^2 \,\Omega_e}{c \,\omega^2} \cos \theta_{Bk}, \qquad \rho_W = \frac{\omega_p^2 \,\Omega_e^2}{2c \,\omega^3} \sin^2 \theta_{Bk}, \tag{18}$$

with  $\cos \theta_{Bk} \equiv B_{\parallel}/B$  taken as signed, so the sign of  $\rho_R$  is set by the line-of-sight field component  $B_{\parallel}$ . These expressions apply only along the escape path outside the thin ECME growth layer and not inside the resonant maser zone ( $\omega \simeq n\Omega_e$ ).

In quasi-transverse propagation ( $\theta_{Bk} \approx 90^{\circ}$ ), which is appropriate for LPRTs, the rotation coefficient  $\rho_R$  becomes very small while the conversion coefficient  $\rho_W$  remains finite. Faraday conversion therefore dominates over rotation, and neglecting  $\rho_R$  gives the pure-conversion limit. With the Q axis defined along the sky-projected  $\mathbf{B}$ , the transfer equations re-

duce to

$$\frac{dQ}{ds} = 0, \qquad \frac{dU}{ds} = \rho_W V, \qquad \frac{dV}{ds} = -\rho_W U.$$
(19)

These equations describe the mixing between U and V as the wave traverses the plasma slab.

In the case of a small cumulative conversion depth

$$\tau_C \equiv \int_0^{s_{\rm esc}} \rho_W \, ds \ll 1,\tag{20}$$

one obtains the following linearised behaviour at escape:

$$U(s_{\rm esc}) \simeq U_0 + \tau_C V_0$$
,  $V(s_{\rm esc}) \simeq V_0 - \tau_C U_0$ ,

so that an initially purely circular state  $(U_0 = 0, V_0 > 0)$  acquires a small linear component  $U/I \simeq \tau_C$ .

On the other hand, in the regime with  $\tau_C \sim 1$ , conversion is strong and the emerging radiation can be predominantly linear even if the intrinsic maser emission was purely circular. We note that the conversion depth  $\tau_C$  increases with electron density (via  $\omega_p^2$ ), magnetic field strength (via  $\Omega_e^2$ ), path length, and toward lower  $\nu$  (as  $\omega^{-3}$ ) in the cold-plasma, high-frequency limit used here.

To illustrate the polarisation evolution, we now integrate the reduced Stokes system (eqs. 14) for a uniform slab of thickness L, in which  $\rho_W$  and  $\rho_R$  are held constant along the ray (constant within each run, varied between runs), with  $S_I = 0$ ,  $\eta_I L \ll 1$ ,  $\rho_W$  and  $\rho_R$  taken from eqs. 18, and  $\theta_{Bk} = 85^{\circ}$ , so that  $\rho_R$  is small but not equal to zero.

The initial conditions  $(I_0, Q_0, U_0, V_0) = (1, 0, 0, 1)$  represent 100 per cent circular ECME at the base of the propagation region, which correspond to s = 0. For the runs shown in Fig. 3 we vary  $n_e$  and  $\nu_{\rm obs}$  through their appearance in  $\rho_W$  and  $\rho_R$ .

For LPRTs, the cumulative rotation depth  $\tau_R$  (eq. 11) is typically much smaller than  $\tau_C$  at GHz frequencies because  $\rho_R \propto \omega^{-2}$  whereas  $\rho_W \propto \omega^{-3}$ , and because escape occurs close to  $\theta_{Bk} \approx 90^\circ$  where  $\cos\theta_{Bk}$  (and hence  $\rho_R$ ) is strongly suppressed (see eqs. 18). Nevertheless, a small non-zero  $\tau_R$  produces mild Q/I excursions in the numerical solutions, as seen in Fig. 3, even though conversion still dominates the overall evolution of the polarisation fractions.

These results clearly illustrate how modest changes in the magnetised plasma drive the transition from predominantly circular to predominantly linear output. To conclude, ECME does not prescribe a unique polarisation state. Instead, it can produce emission ranging from nearly purely circular to predominantly linear, set by the local density, the viewing geometry, and the characteristics of the magnetised plasma through which the escaping wave propagates.

## 3.2 Application to LPRTs

There are several classes of astrophysical sources that show highly polarised radio pulses that can be explained in terms of ECME. Some are binary systems, such as the WD pulsars, whose prototype is AR Scorpii (Marsh et al. 2016). In these systems, a MWD interacting with its companion exhibits coherent, strongly polarised emission. These WD pulsars are phenomenologically similar to MCVs, long recognised as ECME emitters (for the first identification of ECME as a possible emission mechanism in MCVs, see Chanmugam & Dulk 1982). These interacting magnetic binaries demonstrate that compact, magnetised stars can produce auroral

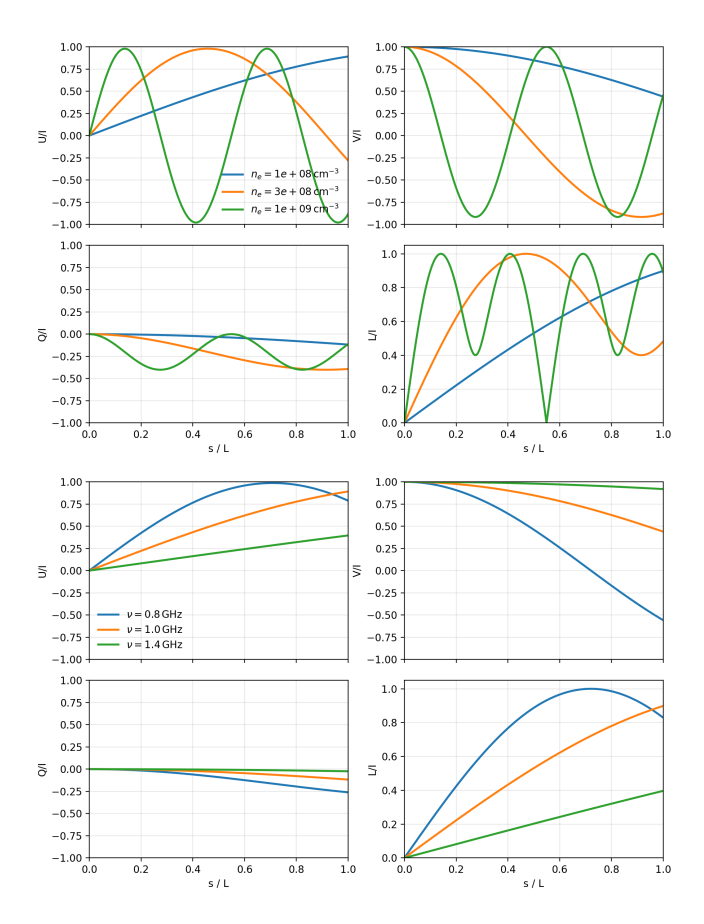


Figure 3. Propagation induced evolution of the polarisation fractions in a cold, low loss, quasi transverse escape layer. Each panel shows U/I, V/I, Q/I, and  $L/I = \sqrt{Q^2 + U^2}/I$  as functions of s/L for an initially circularly polarised state  $(I_0 = 1, Q_0 = U_0 = 0, V_0 = 1)$ . Top panel: Density sweep with  $n_e = \{10^8, 3 \times 10^8, 10^9\}$  cm<sup>-3</sup> at fixed  $\nu_{\rm obs} = 1$  GHz and  $\theta_{Bk} = 85^\circ$ . Both  $\rho_W$  and  $\rho_R$  scale linearly with  $n_e$ , so higher densities produce faster  $U \leftrightarrow V$  oscillations and slightly larger Q/I excursions. Bottom panel: Frequency sweep with  $\nu_{\rm obs} = \{0.8, 1.0, 1.4\}$  GHz at fixed  $n_e = 10^8$  cm<sup>-3</sup> and  $\theta_{Bk} = 85^\circ$ . Increasing frequency weakens the mixing  $(\rho_W \propto \nu^{-3}, \rho_R \propto \nu^{-2})$ , yielding slower conversion, smaller Q/I amplitudes, and reduced growth of L/I at higher  $\nu_{\rm obs}$ .

radio beams (Barrett et al. 2020). However, these are well established binary systems and typically display obvious multiwavelength counterparts.

On the other hand, LPRTs are apparently isolated sources that possess periods of minutes to hours, have narrow radio duty cycles, show large and variable polarisation fractions, and, in most cases, lack a persistent optical/IR/X-ray counterpart. Phenomenologically, they share some properties with main-sequence radio pulse emitters (MRPs, Leto et al. 2021) in that the stable magnetosphere modulates a narrow beam powered by an electron cyclotron maser (e.g., in CU Virginis Trigilio et al. 2011; Ravi et al. 2010). However, the energies of MRPs are several orders of magnitude lower than those of typical LPRTs, whose energetics seem to reflect the much deeper gravitational potential wells of compact stars.

In what follows, we examine whether the LPRTs can be interpreted in terms of ECME.

Table 1 lists the LPRTs that satisfy our criteria: long, repeating radio periods and no detected binary companion.

At present, the only source with confirmed, nearly phase-aligned X-ray emission is ASKAP/DART J1832-0911, whose  $\sim 2\,\mathrm{min}$  X-ray pulses every  $\sim 44\,\mathrm{min}$  demonstrate that isolated LPRTs may not strictly be radio only emitters. We also list GCRT J1745-3009 (Roy et al. 2010) as a historical LPRT candidate. The observed diversity among LPRTs is fully consistent with the ECME framework. In what follows, we examine the sources listed in Table 1 and interpret their observed properties within this framework.

- ASKAP J1755 2527: the bright state shows up to nearly  $\sim$  90 per cent linear polarisation with a flat EVPA curve, consistent with propagation through a low-rotation escape layer. Circular fractions of the order of 25 per cent imply a moderate conversion depth ( $\tau_C \sim 0.1-1$ ), so that intrinsic circular ECME is only partially converted into linear. The weak state becomes more circular, consistent with a reduced magnetised plasma column above the ECME layer or a small change in the field orientation that lowers the effective  $\rho_W$ . The bright state shows the presence of very faint pre- and post-cursor bursts flanking the main pulse. These can be produced as the line of sight grazes different parts of the hollow ECME cone or adjacent field-line bundles.
- GLEAM-X J1627 5235: the bursts show high linear polarisation (up to nearly  $\sim 90$  per cent) and no detectable circular component across a broad frequency range. The EVPA is stable, indicating emission from an ordered field region. Such nearly pure linear output arises when the post-growth propagation occurs through plasma with conversion depths  $\tau_C \gtrsim 1$ , so that intrinsic circular ECME is efficiently converted into linear. The occasional appearance of short  $< 0.5 \,\mathrm{s}$  sub-bursts versus smoother  $30-60 \,\mathrm{s}$  profiles can be attributed to rotation sweeping the line of sight across different sections of the ECME's cone surface: compact regions with strong loss-cone inversion produce narrow bright spikes, while broader bundles yield smooth profiles. The overall behaviour is consistent with emission escaping through moderately dense magnetospheric plasma that generates strong Faraday conversion.
- $\mathbf{GPM} \, \mathbf{J} 1839 10$ : the extreme pulse-to-pulse variability, with L/I ranging from nearly zero to  $\sim 100$  per cent and V/I up to  $\sim 95$  per cent can be produced when the escaping radiation traverses plasma with  $\tau_C \lesssim 1$ . Moderate  $\rho_W$  then partially converts intrinsic circular ECME. Small pulse-topulse changes in density or field orientation along neighbouring rays alter the balance between U and V, generating pulses that switch between strongly circular and predominantly linear. The observed sign reversals in V and the presence of orthogonal polarisation modes follow from a small but nonzero  $\rho_R$  combined with variations in the projected magneticfield geometry across the emission region. The down-drifting substructures arise as rotation sweeps the line of sight across different parts of the resonance surface. This happens because  $\nu \propto B_{\rm loc}(r)$ , so that higher frequencies originate at smaller radii and lower frequencies at larger radii, producing a systematic drift to lower  $\nu$  with time. Distinct fieldline bundles can therefore give multiple drifting rates. Broad components arise when the line of sight intersects a fieldline bundle over a wide range of radii, so that emission from many neighbouring resonance layers, each with a slightly different  $B_{loc}(r)$ , overlaps in time and frequency. By contrast, the narrowband elements originate from much more spatially

Table 1. Observed properties of the LPRTs. The periods P and duty cycles  $\Delta t/P$  are taken from the discovery papers. Peak flux densities and observing frequencies refer to the brightest reported bursts. Distances are derived from Galactic electron-density models and may be uncertain by a factor of  $\sim 2$  (e.g. Yao et al. 2017).

Object	Period	Distance (kpc)	$\mathbf{Multi}\text{-}\lambda$	Polarisation / radio behaviour
ASKAP J1755 – 2527				
McSweeney et al. (2025), Dobie et al. (2024)	1.16 h	4.7	Radio only	Bright pulses show $\sim 90$ per cent linear polarisation with a flat EVPA curve and $\sim 25$ per cent circular. A weaker state becomes more circularly polarised. Very faint pre- and post-cursor pulses flank the main pulse. Duty cycle is $\sim 2.8$ per cent; month-scale "on/off" episodes.
ASKAP J1935 + 2148	52 0 main	4.85	Dadia anlu	Two relevisation states Dright model linear un
Caleb et al. (2024)	53.8 min	4.00	Radio only	Two polarisation states. Bright mode: linear up to $\sim 90$ per cent with weak circular. Weak mode: strongly circular ( $\gtrsim 70$ per cent). Pulse "nulling" and mode changes; duty cycle $0.3-1.5$ per cent.
GLEAM-X J1627 – 5235	10 10	19   05	D. Hl.	Linear and the CO man and mith an intertable in
Hurley-Walker et al. (2022)	18.18 min	$1.3 \pm 0.5$	Radio only	Linear up to $\sim 90$ per cent with no detectable circular. Stable EVPA after RM correction. Bursts alternate between short ( $< 0.5 \mathrm{s}$ ) sub-bursts and smoother $30-60 \mathrm{s}$ profiles. Duty cycle $0.9-2.7$ per cent.
GPM J1839 - 10				
Hurley-Walker et al. (2023)	21.97 min	$5.7 \pm 2.9$	Radio only	Extreme pulse-to-pulse variability. Linear fraction $0-100$ per cent; circular up to $\sim 95$ per cent with sign reversals. Orthogonal polarisation modes detected. Short-duration sub-bursts with single- and multi-component down-drifting ( $\sim 5-17 \text{ MHz ms}^{-1}$ ). Duty cycle $2.3-22.7$ per cent; highly intermittent over decades.
$\rm ASKAP/DARTJ1832-0911$				
Li et al. (2024), Wang et al. (2025)	44 min	$\sim 4.6$	Radio and X-ray	Linear fractions approaching $\sim 100$ per cent with a small, phase-locked circular component. Radio and X-ray pulses nearly phase-aligned. Duty cycle $\sim 4.5$ per cent.
ASKAP J1839 – 0756	0.45.1	40110	D 1: 1	
Lee et al. (2025)	6.45 h	$4.0 \pm 1.2$	Radio only	Two pulses separated by half a rotation. Main pulse: mixed linear (up to $\sim 80$ per cent) and circular (up to $\sim 40$ per cent) with a sign change. Interpulse: $\sim 90$ per cent linear with negligible circular. Pulse width broader at 816 MHz than at 2.2 GHz; quasi-periodic $\sim 2.4$ s fine structure. Duty cycle $\lesssim 1$ per cent; "on/off" behaviour.
Historic candidate:				v v · · ~ F · · · · · , · · · · · · · · · · · · ·
GCRT J1745 - 3009				
Hyman et al. (2005), Roy et al. (2010)	77 min	1 - 8.5	Radio only	Circular up to 100 per cent. Sporadic, irregular bursts. Duty cycle $10 - 13$ per cent. Switch between "on" and "off" modes.

confined regions within a bundle, where the loss-cone inversion is strongest over only a small radial interval, producing emission concentrated in a tighter frequency band. Bundles located further from the magnetic axis start at lower frequencies and drift more steeply, reproducing the multicomponent behaviour seen in this source.

• ASKAP J1935 + 2148: this source shows two distinct polarisation states. In the bright mode, linear fractions approach  $\sim 90$  per cent, consistent with escape through plasma where the cumulative conversion depth is  $\tau_C \sim 0.1 - 1$  (up to a few), so that  $\rho_W$  dominates and only small Q/I fluctuations arise from a weak but non-zero  $\rho_R$ . In the weak mode, the emission becomes strongly circular (greater than 70 per cent),

indicating that the escaping radiation encounters plasma with very small  $\tau_C$ , so that only limited conversion of the intrinsic circular ECME occurs. The transition between these two polarisation regimes follows from rotation-driven or inflow-driven changes in the magnetised plasma column above the ECME layer, altering the local density and field geometry traversed by the escaping beam.

• ASKAP/DART J1832 - 0911: the nearly phase-aligned radio and X-ray pulses show that the same magneto-spheric region supplies both the energetic electrons and the ECME layer. The extremely high linear fractions (approaching 100 per cent), together with a phase-locked circular component and a narrow duty cycle, are consistent with ECME

escaping through plasma with  $\tau_C \sim 1$  and  $\tau_R \ll 1$ . To produce the observed X-ray luminosity, the accretion rate (see Sec. 4) must be sufficiently high to power the X-ray hotspot and supply the outer magnetosphere with the plasma column required for conversion, but also remaining low enough that absorption  $(\eta_I L)$  stays small enough to allow the maser beam to escape.

- ASKAP J1839 0756: the very long period ( $P \simeq$ 6.45 h), the presence of a bright main pulse and a weaker interpulse separated by roughly half a rotation, and the distinct EVPA-swing characteristics indicate an oblique rotator in which emission from both magnetic poles intersect the line of sight. In the ECME picture, the main pulse exhibits mixed linear and circular polarisation with a sign reversal in V. This arises when the escaping radiation traverses plasma where  $\rho_W$  is appreciable, so that only part of the intrinsic circular ECME is converted into linear, while the changing field orientation across the pulse window alters the projected handedness and produces the observed V-sign change. Instead, the interpulse is almost purely linear, implying a line of sight that intersects the hollow-cone beam at the opposite pole where the local plasma conditions yield strong conversion ( $\rho_W$  large).
- GCRT J1745 3009 (historic candidate): the nearly 100 per cent circular bursts require that Faraday conversion along the escape path be very weak, consistent with ECME escaping along low density columns where  $\rho_W$  is small and any rotation conversion coupling is negligible.

## 4 INTERACTION WITH THE ENVIRONMENT

LPRTs require an explanation for (i) how neutron stars can attain spin periods of minutes to hours, and (ii) how they maintain the non-thermal electron populations needed for coherent emission. Vacuum dipole braking alone cannot spin pulsars down to such long periods within Galactic timescales. At the same time, rotational energy losses at these long P are negligible, so an external power source is needed to sustain the electron cyclotron maser.

In what follows, we examine how interaction with the ISM can satisfy both conditions. We first show how magnetospheric torques from captured ISM material can drive neutron stars from ordinary pulsar periods to  $P \sim 10^2 - 10^4$  s, and then demonstrate how the same ISM inflow can supply both the particles and the energy reservoir required to sustain ECME at kiloparsec distances.

## 4.1 Origin of long-period neutron stars

Neutron stars are typically born with  $P_0 \sim 0.03-0.3\,\mathrm{s}$  and  $B_* \sim 10^{11}-10^{13}\,\mathrm{G}$ , so attaining periods of minutes to hours requires additional spin-down.

Vacuum dipole braking alone is insufficient. Under the standard dipole assumptions of braking index n=3, constant  $B_*$ , negligible initial period  $(P_0 \ll P)$ ,  $I=10^{45}\,\mathrm{g\,cm^2}$ ,  $R_*=10^6\,\mathrm{cm}$ , and  $B_*=10^{12}\,\mathrm{G}$ , the dipole spin-down timescale becomes

$$\tau_{\rm dip} \approx 1.7 \times 10^{13} \left(\frac{P}{10^3 \,\rm s}\right)^2 \,\rm yr,$$
(21)

so reaching  $P \sim 10^3$  s would exceed a Hubble time.

A faster channel is early supernova fallback (e.g. Alpar et al. 2001). Accretion from a disc or torus can spin the neutron star down from seconds to  $10^3 - 10^4$  s within  $10^3 - 10^5$  yr, acting while the external dipole is still relatively strong and simultaneously burying it to  $B_* \sim 10^8 - 10^{10}$  G. Such fields favour ECME because they more readily satisfy  $\omega_p/\Omega_e \lesssim 0.3$  in the maser-emission region (see Section 4.2).

A slower but still viable route is long-term interaction with the ISM (e.g. Prokhorov et al. 2002). A neutron star of mass M and velocity v moving through gas of electron density  $n_e$  captures material at the rate

$$\dot{M} \simeq 4\pi G^2 M^2 m_p \, n_e \, v^{-3}.$$
 (22)

For  $M = 1.4 M_{\odot}$  the corresponding capture rate is

$$\dot{M} \simeq 7.3 \times 10^8 \left(\frac{n_e}{1 \, \mathrm{cm}^{-3}}\right) \left(\frac{v}{100 \, \mathrm{km \, s}^{-1}}\right)^{-3} \, \mathrm{g \, s}^{-1},$$

so for  $n_e = 1 - 10 \,\mathrm{cm}^{-3}$  we obtain  $\dot{M} \simeq (0.7 - 7.3) \times 10^9 \,\mathrm{g \, s}^{-1}$ . If the Alfvén radius  $R_A$  lies outside the corotation radius, the rotating magnetosphere applies a propeller-like torque,

$$I\dot{\Omega} \simeq -\dot{M}\,\Omega\,R_A^2,$$
 (23)

where

$$R_A \simeq 3.2 \times 10^{10} \left(\frac{B_*}{10^{12} \,\mathrm{G}}\right)^{4/7} \left(\frac{R_*}{10^6 \,\mathrm{cm}}\right)^{12/7}$$

$$\times \left(\frac{M}{1.4 \,M_\odot}\right)^{-5/7} \left(\frac{n_e}{1 \,\mathrm{cm}^{-3}}\right)^{-2/7} \left(\frac{v}{100 \,\mathrm{km \, s}^{-1}}\right)^{6/7} \,\mathrm{cm}.$$
(24)

The spin evolution follows

$$\Omega(t) = \Omega_0 e^{-t/\tau_{\text{prop}}}, \qquad \tau_{\text{prop}} = \frac{I}{\dot{M}R^2}.$$
 (25)

Using Eqs. 22 and 24, the characteristic timescale becomes

$$\tau_{\text{prop}} \approx 4.2 \times 10^7 \left(\frac{I}{10^{45} \,\text{g cm}^2}\right) \left(\frac{B_*}{10^{12} \,\text{G}}\right)^{-8/7} \left(\frac{R_*}{10^6 \,\text{cm}}\right)^{-24/7} \\ \times \left(\frac{M}{1.4 \,M_\odot}\right)^{-4/7} \left(\frac{n_e}{1 \,\text{cm}^{-3}}\right)^{-3/7} \left(\frac{v}{100 \,\text{km s}^{-1}}\right)^{9/7} \,\text{yr.}$$
(26)

For the fiducial parameters  $B_*=10^{12}\,\rm G,\,M=1.4\,M_\odot,\,R_*=10^6\,\rm cm,\,I=10^{45}\,\rm g\,cm^2,\,and\,}n_e=1-10\,\rm cm^{-3},\,this$  gives

$$\tau_{\text{prop}} \approx (1.6 - 4.2) \times 10^7 \,\text{yr}.$$

For the same parameters, Eq. 24 gives  $R_A \simeq (1.7-3.2) \times 10^{10} \, \mathrm{cm}$ 

Integrating Eq. 23 yields the time to evolve from  $P_0 = 0.5$  s to P:

$$t = \tau_{\text{prop}} \ln \left( \frac{P}{P_0} \right), \tag{27}$$

so achieving  $P = 10^3 - 10^4$  s requires  $t \sim (1-4) \times 10^8$  yr, well within the age of the Galaxy.

# 4.2 Injection of non-thermal electrons and the ISM power supply

Coherent radio bursts in LPRTs require a persistent supply of mildly relativistic electrons. For slowly rotating neutron stars, a natural and sustainable source of such particles is weak accretion from the surrounding ISM.

Accretion from the ISM onto old, isolated neutron stars was first proposed by Ostriker et al. (1970) and later revisited by Treves & Colpi (1991) and Blaes & Madau (1993) as a possible source of faint soft X-ray emission detectable with the ROSAT All-Sky Survey. However, no secure population of such objects emerged (Colpi et al. 1998). Subsequent work demonstrated that the classical Bondi-Hoyle estimate systematically overpredicts the luminosity because it neglects magnetic and rotational effects that strongly inhibit inflow (e.g. Perna et al. 2003). MHD simulations confirm that the magnetosphere can substantially reduce the accretion rate relative to the Bondi-Hoyle value, either through magnetic pressure or propeller action (Romanova et al. 2003; Toropina et al. 2012). The resulting luminosities are expected to be only  $10^{28} - 10^{29} \,\mathrm{erg}\,\mathrm{s}^{-1}$ , well below the detection thresholds of all-sky surveys for sources located beyond a few hundred parsecs.

Nonetheless, the quasi-simultaneous radio and X-ray pulses detected from ASKAP/DART J1832 - 0911 strongly suggest that an ISM-driven accretion channel can operate in at least some old, isolated neutron stars. The same systems may therefore manifest as LPRTs, with coherent ECME powered by the weak inflow that also produces soft X-rays. This provides an observationally supported and physically selfconsistent energy pathway. In this regime, the captured material is funnelled by the stellar magnetic field onto small polar caps, where it is thermalised and emits X-rays. A fraction of the inflowing electrons is instead accelerated along converging field lines, maintaining the anisotropy required for maser amplification. Because the X-rays originate near the magnetic footprints of closed field lines, while the radio emission arises higher up where  $B = B_{loc}$ , the two bands are expected to be nearly phase-aligned, so that the same ISM inflow powers both the soft X-ray component and the ECME bursts.

For a compact object of mass M and radius  $R_*$  moving at velocity v through interstellar gas of electron density  $n_e$ , the Bondi-Hoyle upper bound on the accretion power is

$$L_{\rm acc} \simeq \frac{GM\dot{M}}{R_*} \simeq 1.3 \times 10^{29} \left(\frac{M}{1.4 \, M_{\odot}}\right)^3 \left(\frac{R_*}{10^6 \, \rm cm}\right)^{-1} \times \left(\frac{n_e}{1 \, \rm cm^{-3}}\right) \left(\frac{v}{100 \, \rm km \, s^{-1}}\right)^{-3} \, \rm erg \, s^{-1}.$$
 (28)

For typical interstellar densities  $n_e \sim 1-10\,\mathrm{cm}^{-3}$  and velocities  $v \sim 30-100\,\mathrm{km\,s}^{-1}$ , the Bondi-Hoyle estimate gives  $L_{\rm acc} \sim 10^{29}-10^{31}\,\mathrm{erg\,s}^{-1}$ . Magnetic pressure and rotational inhibition reduce the actual inflow by factors of  $10^{-2}-10^{-3}$  (Blaes & Madau 1993; Toropina et al. 2012), leaving an effective luminosity of  $\sim 10^{28}-10^{29}\,\mathrm{erg\,s}^{-1}$ , which is sufficient to power both ECME and a soft X-ray hotspot.

## 4.3 Power budget and a velocity ceiling

Let  $f_b$  be the beaming fraction and  $\eta_r$  the efficiency for converting the total accretion power into coherent radio emission. Requiring the available accretion power to exceed the emitted radio power gives

$$L_{\rm acc} \ge \frac{f_b L}{n_c},$$
 (29)

which, combined with Eq. 28, yields an explicit upper limit on the stellar velocity:

$$v \le 100 \left[ \frac{1.3 \times 10^{29} \, \eta_r \, n_e}{f_b \, L} \right]^{1/3} \, \text{km s}^{-1}$$

$$\simeq 35 \left( \frac{L}{10^{31} \, \text{erg s}^{-1}} \right)^{-1/3} \left( \frac{f_b}{0.03} \right)^{-1/3} \left( \frac{\eta_r}{0.1} \right)^{1/3} \left( \frac{n_e}{1 \, \text{cm}^{-3}} \right)^{1/3} \, \text{km s}^{-1}.$$
(30)

For representative values  $L=10^{31}\,\mathrm{erg\,s^{-1}},\ f_b=0.03,$  and  $\eta_r=0.1,$  this yields  $v\lesssim 35\,n_e^{1/3}\,\mathrm{km\,s^{-1}},$  i.e.,  $\sim 35\,\mathrm{km\,s^{-1}}$  for  $n_e=1\,\mathrm{cm^{-3}}$  and  $\sim 75\,\mathrm{km\,s^{-1}}$  for  $n_e=10\,\mathrm{cm^{-3}}$ . Hence, only slowly moving neutron stars embedded in moderately dense interstellar regions can satisfy the power budget.

## 4.4 Accretion versus propeller

Whether accretion proceeds or is inhibited by the propeller effect depends on the relative positions of the Alfvén and corotation radii. Accretion occurs when

$$R_A < R_{\rm co}, \qquad R_{\rm co} = \left(\frac{GM}{\Omega^2}\right)^{1/3}.$$
 (31)

Because  $\dot{M} \propto n_e v^{-3}$ , this condition defines an upper limit to  $B_*$  for given  $(P, n_e, v)$ . For  $B_* \sim 10^8 - 10^{10} \, \mathrm{G}$  and  $P \sim 10^3 - 10^4 \, \mathrm{s}$ , one finds  $R_A < R_{\rm co}$  over a broad region of parameter space  $(n_e = 1 - 10 \, \mathrm{cm}^{-3}, \, v \lesssim 80 \, \mathrm{km \, s}^{-1})$ , allowing matter to reach the surface and release accretion luminosities of  $L_{\rm acc} \sim 10^{29} - 10^{31} \, \mathrm{erg \, s}^{-1}$ .

For higher magnetic fields ( $B_* \gtrsim 10^{12} \, \mathrm{G}$ ) at comparable spin periods,  $R_A > R_{\rm co}$  and accretion is centrifugally inhibited (propeller regime). In this case the maximum available power is limited to the work done near  $R_A$ :

$$L_{\text{max}} \simeq \frac{GM\dot{M}}{R_A} \simeq 3 \times 10^{28} \left(\frac{B_*}{10^{12} \,\text{G}}\right)^{-4/7} \left(\frac{n_e}{1 \,\text{cm}^{-3}}\right)^{9/7} \times \left(\frac{v}{100 \,\text{km s}^{-1}}\right)^{-27/7} \,\text{erg s}^{-1}.$$
(32)

Allowing for a leakage fraction  $f_{\rm leak} \lesssim 10^{-3}$ , representing the small portion of inflowing material that penetrates the centrifugal barrier through magnetic reconnection or Kelvin-Helmholtz instabilities at the magnetospheric boundary (e.g. Romanova et al. 2003), gives an effective luminosity  $L_{\rm eff} \simeq f_{\rm leak} L_{\rm max} \sim 10^{26} - 10^{27} \, {\rm erg \ s^{-1}}$ , which is insufficient to sustain detectable ECME or X-ray emission beyond a few hundred parsecs.

## 4.5 ECME viability and the neutron star versus MWD central engine

Taken together, Sections 4.2, 4.3, 4.4 show that the most plausible ECME LPRTs are long-period, relatively low-field neutron stars moving slowly through moderately dense interstellar gas. In this picture, the captured ISM inflow powers thermal X-rays at the magnetic footprints, while the same field-line bundle channels non-thermal electrons to the high-altitude ECME layer, allowing radio and X-ray pulses to appear nearly phase-aligned without invoking a companion. The radio/X-ray alignment of ASKAP/DART J1832-0911 is consistent with this interpretation.

The alternative possibility is that some LPRTs might instead be powered by isolated MWD. These objects possess strong magnetic fields ( $B_* \simeq 10^4 - 10^9\,\mathrm{G}$  Ferrario et al. 2020) and have extended magnetospheres capable of sustaining ECME. However, they differ sharply from neutron stars in accretion power, curvature radii, and achievable luminosities. We therefore examine whether a MWD can satisfy the same geometric and energetic requirements.

Isolated MWDs might, in principle, appear as LPRTs, particularly because the much larger magnetospheres of MWDs yield lower plasma densities at comparable inflow rates, thus making the maser condition  $\omega_p/\Omega_e \lesssim 0.3$  easier to satisfy. The difficulty lies in the available power: even under optimistic ISM accretion, a MWD with  $B_* \sim 10^8$  G,  $M \simeq 0.8\,M_\odot$ , and  $R_* \simeq 10^9$  cm can only supply  $L_{\rm acc} \sim 10^{26}-10^{27}\,{\rm erg\,s^{-1}}$ , several orders of magnitude below the radio luminosities inferred for LPRTs (see Eq. 28). Thus, while ECME may occur at low levels, the emission from MWDs would be too weak to be detected beyond a few hundred parsecs.

We also note that in a dipolar magnetic field the local radius of curvature quantifies how sharply a field line bends in the meridional plane. It is given by (Gangadhara 2004)

$$R_{\rm c} = \frac{r(1+3\cos^2\theta)^{3/2}}{3\sin\theta(1+\cos^2\theta)},\tag{33}$$

which reduces to  $R_{\rm c} \simeq r/3$  at the magnetic equator. A smaller  $R_{\rm c}$ , therefore, corresponds to a more tightly curved field line and a faster change in the local magnetic-field direction along that line. At fixed  $B_{\rm loc}$  one has  $R_{\rm c} \propto R_* B_*^{1/3}$ , so any neutron star possesses a curvature radius orders of magnitude smaller than that of a MWD.

To give some illustrative examples, for ECME at  $\nu_{\rm obs} \simeq 1\,{\rm GHz}~(B_{\rm loc} \simeq 357\,{\rm G})$  in a MWD with  $B_* = 10^8\,{\rm G}$ , the resonance condition places the emitting layer at  $r \simeq 6.5 \times 10^{10}\,{\rm cm}$ , giving  $R_{\rm c} \sim 2.2 \times 10^{10}\,{\rm cm}$ . In comparison, a neutron star with  $B_* = 10^{12}\,{\rm G}$  would host the same resonance at  $r \simeq 1.4 \times 10^9\,{\rm cm}$ , yielding  $R_{\rm c} \simeq 5 \times 10^8\,{\rm cm}$ , about fifty times smaller.

For a neutron star with a weaker field of  $B_* = 10^8$  G, the same scaling gives  $R_c \simeq 2.2 \times 10^7$  cm, nearly  $10^3$  times smaller than the MWD value above, reinforcing the expectation of strong rotational modulation and making such low-field neutron stars even more compelling candidates for LPRTs (see below).

The much larger curvature radius in MWDs means that, for small  $\beta$ , the field orientation changes only slowly across the emission region. As a result, the beaming direction varies little during a full rotation, allowing several field-line bundles to satisfy the maser resonance condition simultaneously if the angle between the field and line of sight is favourable. Emission from these extended auroral arcs can therefore overlap in rotational phase, producing a quasi-steady radio signal. For MWDs with large magnetic obliquities ( $\beta \gtrsim 60^{\circ}$ ), however, the field direction at the ECME layer changes significantly as the star rotates, leading to stronger amplitude modulation even if the emission is intrinsically continuous.

Finally, dedicated radio searches have found no evidence for coherent emission from isolated MWDs. A wide VLASS cross-match shows that strong ( $\gtrsim 1-3\,\mathrm{mJy}$  at  $3\,\mathrm{GHz}$ ) radio emission, whether continuous or pulsed, is virtually absent outside interacting binaries hosting a MWD, while the most sensitive targeted observations of isolated MWDs yield

only non-detections with stringent upper limits (Pelisoli et al. 2024; Zhang et al. 2025).

In close binaries containing a MWD, magnetic interaction with the companion can create multiple maser sites with differing field orientations and time-variable beaming due to orbital motion and asynchronous rotation. These effects enlarge the effective beaming solid angle and make ECME far more detectable, consistent with the comparatively higher incidence of coherent radio emission among MWDs in interacting systems.

#### 5 DISCUSSION

ECME has not been previously developed as a general framework for the class of isolated LPRTs. On the other hand, old and isolated neutron stars have long been expected to emit soft X-rays through accretion from the ISM (Ostriker et al. 1970).

The discovery of LPRTs may have therefore revealed a previously unrecognised long-P, low- $B_*$  regime in which ECME can operate efficiently, allowing old, isolated neutron stars to be identified and studied as radio sources and, occasionally, as X ray emitters when the inflow from the environment provides sufficient power. In this context, ASKAP J1832 - 0911 may reside in a comparatively dense region of the inner Galactic plane, possibly at the outskirts of a supernova remnant or superbubble, where the ambient gas density and relative velocity can support short-lived episodes of enhanced accretion. The coexistence of ECME bursts and moderate X ray luminosity is therefore not contradictory: ECME is powered by mildly relativistic electrons in the outer magnetosphere of the neutron stars where  $B_{\rm loc} \sim 10^2 - 10^3 \, \rm G$ , whereas the X rays arise from intermittent accretion onto the stellar surface. These systems thus provide a new diagnostic of their surroundings, since the radio luminosity, duty cycle, and occasional X ray emission depend sensitively on the local ambient density, ionisation state, and relative velocity.

Quasi-periodic fine structure is also consistent with ECME phenomenology. In ASKAP J1839 – 0756, substructure as narrow as 100 ms with a quasi-period of 2.4s has been reported (Lee et al. 2025). Fine structure of this kind is a well-established signature of ECME in many different environments. Auroral kilometric radiation from the Earth also shows richly structured, rapidly varying dynamic spectra (Treumann 2006; Taubenschuss et al. 2023). Jupiter's decametric emission displays narrowband drifting elements (Zarka 1998), while solar coherent radio bursts exhibit sub-second spikes and fine structure, interpreted as signatures of small-scale ECME in active-region magnetic loops (e.g. White et al. 2024).

There are also clear limitations to the way we have discussed this emission mechanism. We have assumed centred dipoles and cold-plasma propagation. Multipolar fields or warm-plasma corrections will introduce additional complexity. Time-dependent inhomogeneities or structured inflow have not been discussed explicitly, but are likely to influence both visibility and polarisation. A further limitation is that we have implicitly adopted a loss-cone anisotropy to drive the maser, as naturally occurs in converging magnetospheric fields. In planetary auroral zones, ECME is often powered by a "horseshoe" (or shell) distribution generated by

field-aligned acceleration (e.g. Ergun et al. 2000; Treumann 2006). It is not clear whether isolated neutron stars can develop comparable acceleration structures, but the required kinetic modelling is beyond the scope of this work. A fully self-consistent treatment would require integrating maser growth, three-dimensional simulations of the type conducted by Leto et al. (2016), and frequency-dependent ray propagation.

Despite these caveats, the overall picture holds together. Geometry, polarisation, intermittency, energetics, fine structure, and downdrift all have natural explanations within an ECME framework. This suggests that long-period neutron stars with comparatively low magnetic fields, low space velocities, and weak ISM accretion may form a previously unrecognised class of coherent radio emitters (and sometimes X-ray emitters), offering new insights into neutron stars' magnetospheres beyond the classical pulsar regime.

### 6 CONCLUSIONS

The properties of LPRTs are naturally explained by ECME operating in the extended magnetospheres of long period neutron stars with comparatively low surface fields. The GHz emission originates where  $B \simeq 10^2-10^3$  G, and the narrow beaming can reproduce the observed pulse morphology and energetics. Intrinsically circular maser emission becomes partially or largely linear through Faraday conversion in the overlying magnetic plasma, accounting for the observed diversity from nearly purely circular to almost entirely linear, depending on the local magnetised plasma conditions along the escape path.

Weak accretion from the ISM can supply the modest power implied by the beamed luminosities when  $R_A \lesssim R_{\rm co}$ . In this context, the nearly phase aligned radio and X ray pulses of ASKAP J1832 - 0911 provide strong observational support. LPRTs may therefore represent the visible subset of long period, weak field neutron stars accreting at low rates from the ISM, with matter reaching the stellar surface while the magnetosphere drives coherent ECME.

In this framework, the observed long-term "on" and "off" behaviour of many LPRTs follows from modest variations in the ISM inflow that shift  $R_A$  inward or outward and alter the leakage fraction, intermittently suppressing or restoring the ECME

The ECME model yields several observational predictions. (i) A weak downward drift of pulse phase with decreasing frequency is expected for emission occurring at radii where  $B \propto r^{-3}$ , producing fractional shifts of order less than 1 per cent across 0.7 to 1.5 GHz, as observed in several LPRTs. (ii) Correlated changes in L/I and V/I with observing frequency follow from  $\rho_W \propto \nu^{-3}$ . (iii) Narrow duty cycles imply beaming fractions  $f_b \sim 0.01-0.1$ , suggesting a large unseen parent population.

## APPENDIX A: ECME ESSENTIALS, RESONANCE, AND GEOMETRY

A key ingredient that allows ECME to operate is the development of a loss-cone anisotropy in the electron velocity distribution, arising in a magnetised plasma where the magnetic field strength B increases toward the stellar surface, causing electrons gyrating about  $\mathbf{B}$  to experience a mirror force.

Decompose the velocity  $\mathbf{v}$  into components parallel  $v_{\parallel}$  and perpendicular  $v_{\perp}$  to  $\mathbf{B}$ , such that  $v = \sqrt{v_{\perp}^2 + v_{\parallel}^2}$ , and introduce the Lorentz factor  $\gamma = (1 - v^2/c^2)^{-1/2}$ .

The first adiabatic invariant, the magnetic moment  $\mu$ , is conserved:

$$\mu = \frac{p_{\perp}^2}{2m_e B} = \text{constant}, \qquad p_{\perp} = \gamma m_e v_{\perp}.$$
 (A1)

In the absence of any large, quasi-static field-aligned potential drops that generate a parallel electric field, the total particle energy is conserved, so  $\gamma$  is locally constant. Since  $\mu$  is constant, an increase in B forces  $v_\perp^2$  to increase,and thus  $v_\parallel^2$  must decrease. The parallel equation of motion along the field line (coordinate s) is :

$$\frac{dp_{\parallel}}{dt} = -\mu \frac{dB}{ds},\tag{A2}$$

where  $p_{\parallel}=\gamma m_e v_{\parallel}$  . The right-hand side of the above equation defines the mirror force

$$F_{\parallel} = -\mu \, \frac{dB}{ds},\tag{A3}$$

which acts opposite to the direction of increasing B, slowing electrons moving into stronger fields.

The pitch angle  $\alpha$  is the angle between the electron's velocity  ${\bf v}$  and the local magnetic field  ${\bf B}$ :

$$\tan \alpha = \frac{v_{\perp}}{|v_{\parallel}|}, \qquad 0 \le \alpha \le \frac{\pi}{2}.$$
(A4)

In a converging magnetic field such as a dipole, electrons either mirror or precipitate depending on  $\alpha$ . Large  $\alpha$  favour magnetic trapping, while small  $\alpha$  lead to loss through precipitation into the stellar atmosphere. The so-called "loss cone" in velocity space consists of those pitch angles that do not mirror. Conservation of the first adiabatic invariant (Eq. A1) gives its boundary:

$$\sin^2 \alpha_{\rm L} = \frac{B}{B_{\rm m}}, \qquad (B_{\rm m} > B),$$

where  $B_{\rm m}$  is the field at the mirror point. Continuous removal of small- $\alpha$  electrons and their replenishment by injection (Section 4.2) produces the pitch-angle population inversion that drives maser growth.

Waves grow when they satisfy the cyclotron resonance with the gyrating electrons. We adopt e>0 for the elementary charge, so that the electron gyrofrequency

$$\Omega_e = \frac{eB}{m_e c},\tag{A5}$$

is strictly positive. The cyclotron resonance condition (e.g. Stix 1992) is

$$\omega - k_{\parallel} v_{\parallel} - \frac{n \,\Omega_e}{\gamma} = 0,\tag{A6}$$

where  $n=1,2,\ldots$  is the cyclotron harmonic number. Here  $k_{\parallel}$  is the component of the wavevector along the magnetic field and  $v_{\parallel}$  the electron's parallel velocity. The product  $k_{\parallel}v_{\parallel}$  represents the Doppler shift of the wave frequency in the electron's guiding-centre frame.

For ECME, maximum growth occurs for quasi-transverse

propagation ( $k_{\parallel}\simeq 0$ ), so the Doppler term becomes negligible and the resonance simplifies to

$$\omega \simeq \frac{n\,\Omega_e}{\gamma}.\tag{A7}$$

Equivalently, in frequency units,

$$\nu \simeq \left(\frac{n}{\gamma}\right) \nu_{ce}, \qquad \nu_{ce} = \frac{\Omega_e}{2\pi} \simeq 2.80 \,\mathrm{MHz} \left(\frac{B}{1\,\mathrm{G}}\right).$$
 (A8)

Hence,  $\nu$  determines the local magnetic field:

$$B_{\rm loc}[\mathrm{G}] \simeq 357 \frac{\gamma}{n} \nu [\mathrm{GHz}].$$
 (A9)

We identify the wave frequency  $\nu = \omega/2\pi$  with the observing frequency  $\nu_{\rm obs}$  at the telescope. Gravitational redshift corrections are negligible at the relevant altitudes.

The propagation angle  $\theta_{Bk}$  between the wavevector  $\mathbf{k}$  (with magnitude  $k \equiv |\mathbf{k}| = 2\pi/\lambda$  for a monochromatic plane wave) and the magnetic field  $\mathbf{B}$  is

$$\cos \theta_{Bk} = \frac{\mathbf{k}}{|\mathbf{k}|} \cdot \frac{\mathbf{B}}{|\mathbf{B}|} = \frac{k_{\parallel}}{k}. \tag{A10}$$

Thus, the quasi-transverse condition corresponds to  $k_{\parallel} \simeq 0$   $(\theta_{Bk} \simeq 90^{\circ})$ , and the quasi-parallel condition to  $k_{\perp} \simeq 0$   $(\theta_{Bk} \simeq 0^{\circ})$ .

Two effects favour quasi-transverse escape. First, the ECME growth rate peaks when the cyclotron resonance ellipse in  $(v_{\perp}, v_{\parallel})$  space (Eq. A6) intersects the loss-cone boundary near  $v_{\parallel} \simeq 0$ , selecting  $k_{\parallel} \simeq 0$ . Second, in a strongly magnetised, low-density plasma, only waves travelling nearly perpendicular to  ${\bf B}$  can escape. Together, these conditions confine the escaping radiation to hollow cones whose axes follow  ${\bf B}$  and whose opening angles satisfy  $\theta_{Bk} \simeq 90^{\circ}$ .

The key parameter controlling both growth and escape is the ratio of the plasma frequency  $\omega_p$  to gyrofrequency,

$$\omega_{\rm p} = \left(\frac{4\pi n_e e^2}{m_e}\right)^{1/2}, \qquad \frac{\omega_{\rm p}}{\Omega_e} \lesssim 0.1 - 0.3,$$
(A11)

for which the emission can propagate quasi-transversely without encountering cut-offs or evanescence (Melrose & Dulk 1982; Hewitt et al. 1982). In this regime, the birefringent coupling coefficients  $(\rho_R, \rho_W)$  that mix the Stokes parameters are small locally, but their cumulative effect along the escape path can still produce significant Faraday conversion between U and V.

Hence both the growth maximum and the transparency window select emission angles close to  $90^{\circ}$ ,

$$\theta_{Bk} = \theta_{\text{cone}} \simeq 90^{\circ} - \delta\theta,$$
 (A12)

producing radiation confined to a thin hollow cone whose axis is parallel to  $\mathbf{B}_{\mathrm{loc}}$  (Eq. A9). The small offset  $\delta\theta$  (a few degrees) depends on  $\omega_{\mathrm{p}}/\Omega_{e}$ , the harmonic number n, and the characteristic electron energy. The cone's wall thickness  $\sigma$  is the angular width over which the ECME growth rate remains appreciable and thus scales with the fractional resonance bandwidth.

$$\sigma \propto \frac{\Delta \nu}{\nu},$$
 (A13)

because a finite  $\Delta\nu$  corresponds to a finite range of angles that satisfy the cyclotron resonance condition.

#### ACKNOWLEDGEMENTS

We wish to thank Dayal Wickramasinghe for helpful discussions.

#### DATA AVAILABILITY

This work has no associated observational data. The codes that generated the illustrative figures will be shared on request.

### REFERENCES

Alpar M. A., Ankay A., Yazgan E., 2001, ApJ, 557, L61
Barrett P., Dieck C., Beasley A. J., Mason P. A., Singh K. P., 2020, Advances in Space Research, 66, 1226

Blaes O., Madau P., 1993, ApJ, 403, 690

Caleb M., et al., 2024, Nature Astronomy, 8, 1159

Chanmugam G., Dulk G. A., 1982, ApJ, 255, L107

Colpi M., Turolla R., Zane S., Treves A., 1998, ApJ, 501, 252

Dobie D., et al., 2024, MNRAS, 535, 909

Ergun R. E., Carlson C. W., McFadden J. P., Delory G. T., Strangeway R. J., Pritchett P. L., 2000, ApJ, 538, 456

Ferrario L., Wickramasinghe D., Kawka A., 2020, Advances in Space Research, 66, 1025

Gangadhara R. T., 2004, ApJ, 609, 335

Hewitt R. G., Melrose D. B., Ronnmark K. G., 1982, Australian Journal of Physics, 35, 447

Hurley-Walker N., et al., 2022, Nature, 601, 526

Hurley-Walker N., et al., 2023, Nature, 619, 487

Hyman S. D., Lazio T. J. W., Kassim N. E., Ray P. S., Markwardt C. B., Yusef-Zadeh F., 2005, Nature, 434, 50

Landi Degl'Innocenti E., Landi Degl'Innocenti M., 1973, Sol. Phys., 31, 299

Lee Y. W. J., et al., 2025, Nature Astronomy, 9, 393

Leto P., Trigilio C., Buemi C. S., Umana G., Ingallinera A., Cerrigone L., 2016, MNRAS, 459, 1159

Leto P., et al., 2021, MNRAS, 507, 1979

Li D., et al., 2024, arXiv e-prints, p. arXiv:2411.15739

Marsh T. R., et al., 2016, Nature, 537, 374

Martin B., Wickramasinghe D. T., 1979, MNRAS, 189, 883

Martin B., Wickramasinghe D. T., 1981, MNRAS, 196, 23

Martin B., Wickramasinghe D. T., 1982, MNRAS, 200, 993

McSweeney S. J., et al., 2025, MNRAS, 542, 203

Melrose D. B., Dulk G. A., 1982, ApJ, 259, 844

Ostriker J. P., Rees M. J., Silk J., 1970, Astrophys. Lett., 6, 179 Pacholczyk A. G., 1976, Radio galaxies: radiation transfer, dynamics, stability, and evolution of a synchrotron plasmon. Pergamon Press, New York

Pelisoli I., et al., 2024, MNRAS, 531, 1805

Perna R., Narayan R., Rybicki G., Stella L., Treves A., 2003, ApJ, 594, 936

Prokhorov M. E., Popov S. B., Khoperskov A. V., 2002, A&A, 381, 1000

Ravi V., et al., 2010, MNRAS, 408, L99

Rea N., et al., 2024, ApJ, 961, 214

Romanova M. M., Toropina O. D., Toropin Y. M., Lovelace R. V. E., 2003, ApJ, 588, 400

Roy S., Hyman S. D., Pal S., Lazio T. J. W., Ray P. S., Kassim N. E., 2010, ApJ, 712, L5

Stix T. H., 1992, Waves in plasmas. AIP Press, Springer-Verlag New York, Inc.

Taubenschuss U., Fischer G., Pisa D., Santolík O., Soucek J., 2023, in Louis C. K., Jackman C. M., Fischer G., Sulaiman A. H., Zucca P., eds, Planetary, Solar and Heliospheric Radio Emissions IX. p. 103089, doi:10.25546/103089

## 12 L. Ferrario

```
Toropina O. D., Romanova M. M., Lovelace R. V. E., 2012, MNRAS, 420, 810
Treumann R. A., 2006, A&ARv, 13, 229
Treves A., Colpi M., 1991, A&A, 241, 107
Trigilio C., Leto P., Umana G., Buemi C. S., Leone F., 2011, ApJ, 739, L10
Wang Z., et al., 2025, Nature, 642, 583
White S. M., Shimojo M., Iwai K., Bastian T. S., Fleishman G. D., Gary D. E., Magdalenic J., Vourlidas A., 2024, ApJ, 969, 3
Wu C. S., Lee L. C., 1979, ApJ, 230, 621
Yao J. M., Manchester R. N., Wang N., 2017, ApJ, 835, 29
Zarka P., 1998, J. Geophys. Res., 103, 20159
Zhang L., et al., 2025, Science China Physics, Mechanics, and Astronomy, 68, 129513
```

This paper has been typeset from a  $T_EX/I^aT_EX$  file prepared by the author.